eTransportation 22 (2024) 100380

Contents lists available at ScienceDirect

eTransportation

journal homepage: www.journals.elsevier.com/etransportation

Simulation of single-layer internal short circuit in anode-free batteries

Nitesh Gupta [a], Shanhai Ge [a], Tatsuro Sasaki [b], Kaiqiang Qin [a], Ryan S. Longchamps [a], Koichiro Aotani [b], Chao-Yang Wang [a,*]

[a] Electrochemical Engine Center (ECEC) and Department of Mechanical Engineering, The Pennsylvania State University, University Park, PA 16802, USA
[b] Nissan Research Center, Nissan Motor Co. Ltd., Natsushima, Yokosuka, Kanagawa 237-8523, Japan

ARTICLE INFO

Keywords:
Anode-free cells
Lithium metal cells
Internal short circuit
Large capacity cells
Modelling
COMSOL
Parametric study
Experimentally validated

ABSTRACT

The lithium metal battery technologies that can fulfil the high energy density goal have grave safety concerns and lead to fire/smoke, leading to battery failure. Out of all the causes of fire, internal short circuits (ISC) are the most common. The ISC safety test is considered a crucial checkpoint for battery design, but the present tests, like nail penetration and ball indentation, lack certainty and reproducibility in declaring battery safety. In light of these experimental limitations, we present an experimentally validated ISC simulation method that can elucidate fundamental mechanisms underlying ISC. The experimental/simulation method isolates the shorted single-layer from the unshorted layers, which helps in scrutinizing ISC and thermal runaway (TR) phenomenon. The present ISC model is flexible and computationally inexpensive compared to other 3D electrochemical thermal coupled (ECT) ISC simulations for a whole battery pack. We show the experimental validation of terminal voltage, short-circuit current, shorting resistance, internal temperature and other derived parameters of an ISC simulation of anode-free cell. Finally, the simulation model was used to do a parametric study for an anode-free battery (AFB) and the effect of cell design, and shorting parameters on ISC was scrutinized.

1. Introduction

Emerging needs for energy-dense battery technologies for automotive and aircraft applications have led to rigorous research in lithium metal anode and anode-free cell chemistry [1–3]. Compared to 100–265 Wh/kg energy density of lithium-ion batteries (LiB) [4,5], 300+ Wh/kg of lithium metal battery (LMB) and anode-free battery (AFB) [6] can not only meet the energy density needs for aircraft application but can also serve for the ideal automotive lifetime standard [7]. In this race to achieve the target lifetimes and energy densities, the research on making them safe needs to catch up. Guo et al. [8], Puthusseri et al. [9], and Lu et al. [10], through differential scanning calorimetry (DSC), show that electrolyte-anode reactions in LMBs lead to high energy release irrespective of the type of cathodes. Studies have established that lithium metal batteries have grave safety concerns and lead to fire, smoke, and explosion when subjected to abusive conditions [11].

In abuse conditions, a battery's temperature increases catastrophically due to immense heat release. This high temperature is highly localised and occurs near the abused area, leading to separator breakdown, smoke, fire hazard, and, eventually, the cells get damaged. Out of all the abuse tests, an internal short circuit (ISC) is most prominent in these batteries because of the formation of Lithium dendrites at the anode [12,13]. During an internal short circuit, a localised current flows through a shorting element, which can be a dendrite, an impurity from a manufacturing defect or physical damage. This localised current is very high and leads to thermal runaway (TR) from localised joule heating. The internal short circuit happens in a single-layer of a large-size battery. It may occur at just one location or multiple locations. This property of ISC makes it very difficult to study experimentally. All the abuse tests designed for assessing battery safety, like ball crush (BC) [14], nail penetration (NP) [15–18], embedding low-melting point materials [19], patch heaters [20], and external short circuit [21], lead to complete multi-layer cell shorting and are often unable to produce quantitative and repeatable results. Although the tests function to check the safety of large-format batteries, the unrepeatability associated with them makes it problematic to do an experimentally validated single-layer shorting simulation. All NP simulations in the literature only validate the voltage drop after a short, which in most cases is a sudden drop to near zero when all the cell layers are penetrated [22]. Zhao et al. [23] and Zavalis et al. [24] simulated ISC in NMC-Gr LiBs but did not experimentally validate the results.

In light of the limitation of test procedures and lack of validation using more fundamental experimental data, we present a new model to

* Corresponding author.
E-mail address: cxw31@psu.edu (C.-Y. Wang).

https://doi.org/10.1016/j.etran.2024.100380
Received 20 September 2024; Received in revised form 7 November 2024; Accepted 10 November 2024
Available online 12 November 2024

Nomenclature

Subscripts

ES	energy source
SC	short circuit

Acronyms

AFB	anode-free battery
BC	ball crush
CC	current collector
ES	energy source
ECT	electrochemical thermal
HP	heating power
ISC	internal short circuit
LiB	lithium-ion battery
LMB	lithium metal battery
LHCE	local high concentration electrolyte
NP	nail penetration
SE	short element
SOC	state of charge
TR	thermal runaway

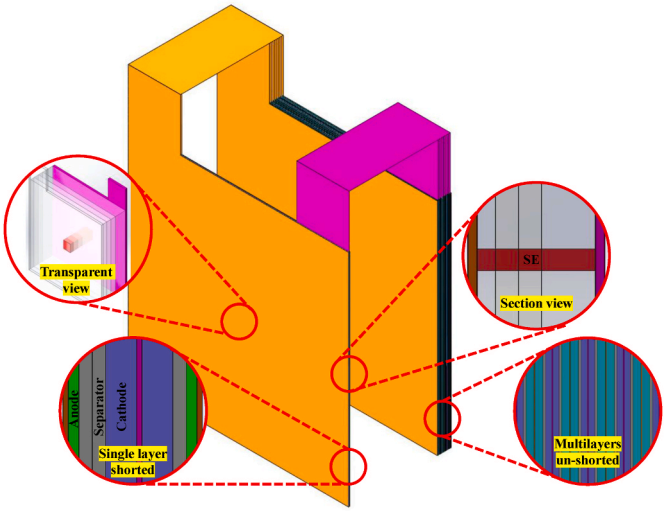

Fig. 1. CAD representation of the ISC Numerical model.

simulate ISC in the present paper. This simulation model can be validated with the novel experimental methodology developed by our group to study the onset of TR during single-layer internal shorting. Fig. 1 shows a 3D CAD for the model used for ISC simulations. In this, a single-layer cell under study, which can be of a chemistry of interest, is shorted internally and is connected in parallel with a LiB energy source. The energy source represents un-shorted layers that are less interesting during an ISC and only serve to supply current to the shorted cell. Thermal insulation is assumed of the shorted cell from the adjacent un-shorted layers in Fig. 1. This can be justified by the short time scales (~3 s) involved in the present study, and the resulting thermal penetration length is estimated to be < 0.3 mm, which is negligibly small as compared to the thickness of the un-shorted layers. Such a configuration helps focus on one layer cell, which is shorted, and the system mimics a full multi-layer battery. With this, it is not only easy to do a parametric study experimentally and numerically, but we can also alter every component of the single-layer shorted cell to see the overall effect on the multi-layer battery. Dividing shorted and unshorted layers working as two separate cells in parallel inherently consumes less computational

Table 1
Electrochemical properties of AFB and LiB.

	Unit	AFB/ Lithium	AFB/ NCM811	LiB/ Graphite	LiB/ NCM811
Exchange current density (i_0)	mA/ cm^2	0.8[a]	0.8[a] ($x^{0.5}$) ($C_e^{0.5}$) $(1-x)^{0.5}$ [25], [b]	0.042[a] ($x^{0.5}$)($C_e^{0.5}$) $(1-x)^{0.5}$ [25] , [b]	0.072[a] ($x^{0.5}$)($C_e^{0.5}$) $(1-x)^{0.5}$ [25] , [b]
Solid diffusivity (D_s)	m^2/s	–	0.368[a] $*10^{-10}$ $((1.5-x)^{1.5})$ [25] , [b]	1.8[a] $*10^{-10}$ $((1.5-x)^{1.5})$ [25] , [b]	1.192[a] $*10^{-10}$ $((1.5-x)^{1.5})$ [25] , [b]
Activation energy for D_s	J/ mol	–	36323[a], [25] , [b]	44568[a] [25] , [b]	17368[a], [25] , [b]
Solid conductivity	S/m	100[c]	3.8[c]	100[c]	3.8[c]
Bruggeman exponent (BE)	–	–	–	2.44[a]	1.87[a]
Transference number	–	0.55 [26] , [a,b]		Fig. 3 , [27] , [a,b]	
Ionic conductivity	S/m	Fig. 1, [26] , [a,b]		Fig. 14 , [27] , [a,b]	
Ionic diffusivity	m^2/s	Fig. 3, [26] , [a,b]		Fig. 13 , [27] , [a,b]	
Activity coefficient	–	1		Fig. 9 , [27] , [a,b]	

[a] fitted.
[b] Literature.
[c] Common value.

power. Focusing on one layer in simulation allows to use a fine mesh for the single-layer shorted cell and a coarse mesh for the unshorted multilayer cell. Conventional 3D multi-scale multi-domain models for multi-layer cells have to use the same mesh for all the layers, which has evidently more mesh elements and, hence, is more computationally expensive.

In section 2 of this study, we present the numerical model and the experimental validation of the charge-discharge characteristics of an anode-free single-layer cell. We also describe the experimental setup for validation of the ISC simulation. In section 3, we present experimental validation results of the ISC simulation of the anode-free single-layer cell shorting assisted by a LiB energy source. We also perform a parametric study to probe the effects of various cell design factors of an anode-free cell on the ISC. In section 4, we conclude the results with a discussion on future applications of the present model.

2. Method

2.1. Numerical model

A 3D electrochemical-thermal (ECT) coupled model was used for the shorted single-layer cell and the energy source. For the electrochemical model, charge and species conservation equations are solved in the electrolyte and solid phase, with their couplings through interfacial charge-transfer reactions defined by Butler Volmer kinetics. All details of the ECT model were given previously [22], and thus, for brevity, are shown in supporting information. The energy equation shown below is also solved to couple the temperature with the electrochemical processes.

$$\frac{\partial(\rho C_p T)}{\partial t} = \nabla . k \nabla T + q_{cell} + q_{short} \quad (1)$$

where q_{cell} is the heat from electrochemical reactions and from potential gradients in the solid and the electrolyte of the single-layer shorted cell, it heats the cell uniformly. q_{short} is the Joule heat (I^2R) generated locally on the shorting object during an ISC. In our study, as most of the shorting current is supplied by the un-shorted multi-layer energy source, the heat from q_{short} is much greater than the q_{cell}, and therefore, the global

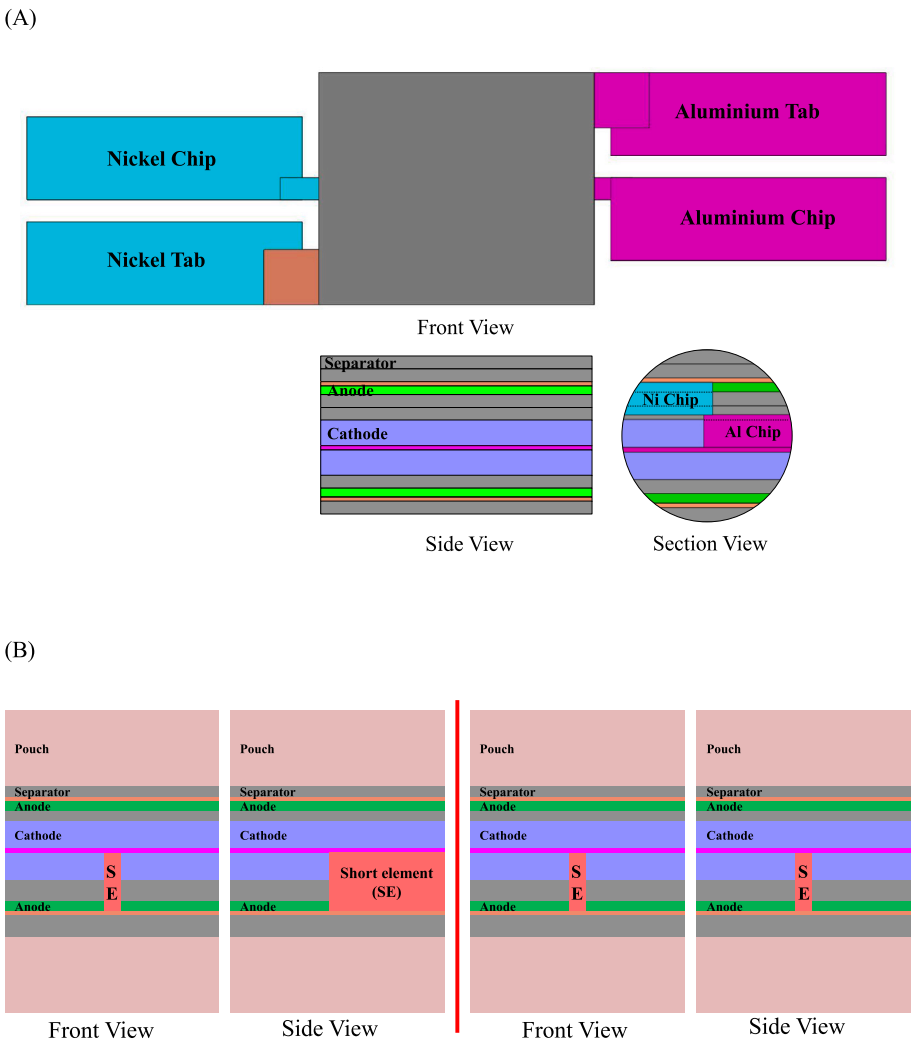

Fig. 2. Schematic representation of (A) single-layer cell used in the experimental setup, (B) simulation setups of the single-layer cell for validation simulations (left) and parametric simulation (right), respectively.

heating of single-layer cell due to q_{cell} is negligible, and solely the effect of localized joule heat from q_{short} can be studied. As a first approximation, we have neglected the effect of lithium metal melting and electrolyte evaporation, as the heat absorbed for these processes is much less than the heat generated during internal short circuits.

A nickel-cobalt-manganese (NCM811) cathode was used for both pouch cells. An anode-free cell was used for the single-layer cell, and a graphite anode cell was used for the energy source. Localized high concentration electrolyte (LHCE) was used for AFB cell, and 1M LiPF6 in EC/EMC (3:7), a commercial electrolyte, was used for the LiB energy source. Tables 1, S1, and S2 show their electrochemical properties, cell designs, and thermal properties. All the electrochemical properties were calibrated using GT-Autolion to match discharge characteristics with experimental data. A multiplication factor was calculated for each cell property so that the error between experimental and numerical discharge data is less. All discharge and ISC simulations were conducted with COMSOL v6.2. The mesh used for single-layer shorted cell layers had 41110 elements, and the mesh for multi-layer unshorted layers had 18200 elements. The results produced in the simulations are mesh-independent. Fig. S1 shows the experimental and simulated discharge curves of 0.13 Ah single-layer AFB with good agreement.

2.2. Experimental setup

Fig. 2A shows a charged anode-free single-layer cell prepared for an ISC experimental study [28]. The experimental cell has four terminals. Two terminals are for anode and cathode current collectors (CC), and two are for the shorting chips in contact with anode and cathode CCs inside the cell. An aluminum chip was pressed with cathode CC by removing the cathode active material coating. A nickel chip was placed against anode CC. The regular cell terminals were connected to an energy source, and the shorting terminals were connected to each other via a switch. When the switch was closed, an equivalent anode CC to cathode CC short happened, and the energy source and single-layer cell supplied current to the short. The instantaneous current was measured at multiple locations using shunt resistors and measuring voltage drop over them. One shunt was placed in series with chip terminals to measure total shorting current (I_{SC}), and another shunt was placed in series with the energy source to measure the current supplied by the energy source (I_{ES}). In this case, the total shorting resistance (R_{SC}) is the addition of the cathode terminal to the cathode chip terminal resistance and the anode terminal to the anode chip terminal resistance. These resistances were measured by measuring the voltage drop across these terminals. Thermocouples were placed inside and outside the cell at multiple locations to measure instantaneous temperature. A data acquisition unit (DAQ) of sampling frequency 8Hz was used to measure

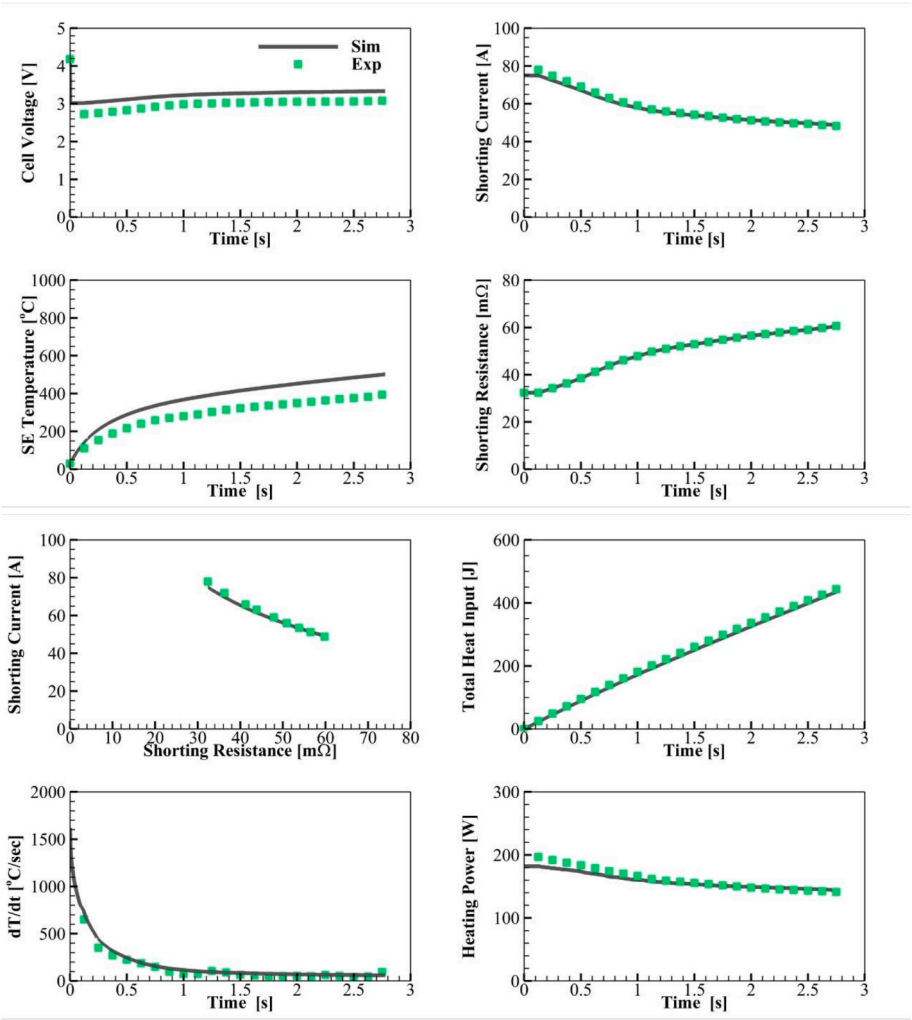

Fig. 3. Comparison of simulation and experimental results for ISC model validation.

voltage drops and temperature data. The single-layer shorted cell was placed in a steel chamber. A GoPro camera was used outside of the chamber to record the whole ISC process through a glass window.

The capacity of the single-layer cell is small and, hence, does not contribute much to the shorting current. This feature of the setup allows the change of single-layer cell material easily, such as lithium metal vs graphite anode, NMC811 vs LFP, liquid vs solid electrolytes and at various states of charge [28].

2.3. Shorting element and total short circuit resistance (R_{SC})

In the present internal short-circuit study for electrochemical cells, the shorting element is an electrically conducting medium which connects the anode CC to the cathode CC. Fig. 2b shows the geometry of the shorting element used in ISC simulations for experimental validation (left) and parametric study (right). The shorting element for validation simulations was modelled as a long strip to match the shorting chips used in the experiment. The shorting element's heat capacity and thermal conductivity were also matched with the chips using a calculated equivalent value. A 4 × 4 mm element as the baseline was modelled as the shorting element for parametric simulations. The thermal properties of lithium were used for this shorting element to mimic actual shorting scenarios.

The total short-circuit resistance value was directly taken from the experimental reading for validation simulation. This value was input to the shorting element as its internal resistance. In parametric simulations, a constant value of internal resistance was chosen based on the contact resistance of the shorting element with anode and cathode CCs, which was given to the shorting element. The calculated internal resistance value based on lithium resistivity was very small and, hence, was not considered. For parametric simulations, the total short circuit resistance was calculated by adding cathode CC internal resistance, anode CC internal resistance, and the shorting element's internal resistance.

3. Results and discussion

3.1. Validation

Fig. 3 shows comparisons between the experiment and the simulation of an ISC in a single-layer anode-free cell, which was connected to a 2.6 Ah LiB in parallel. In the experiment, as soon as the switch was closed, the single-layer cell got short, and the cell's terminal voltage dropped instantaneously to 2.8 V. A similar phenomenon was seen in the simulation where the voltage drops to 3 V. The voltages do not match precisely because of an extra ohmic drop in the cables and contacts involved in the experiment. The enormous current rush was seen soon after shorting, resulting in a large heating rate (dT/dt) and large temperature gradients. As soon as the temperature increased, the internal resistance of metals involved in the shorting circuit increased as they had a positive temperature coefficient of resistance. Shorting resistance at t = 0 sec was 33 mΩ and increased rapidly to 60 mΩ within 3 s. This increase in resistance leads to a decrease in shorting current. The

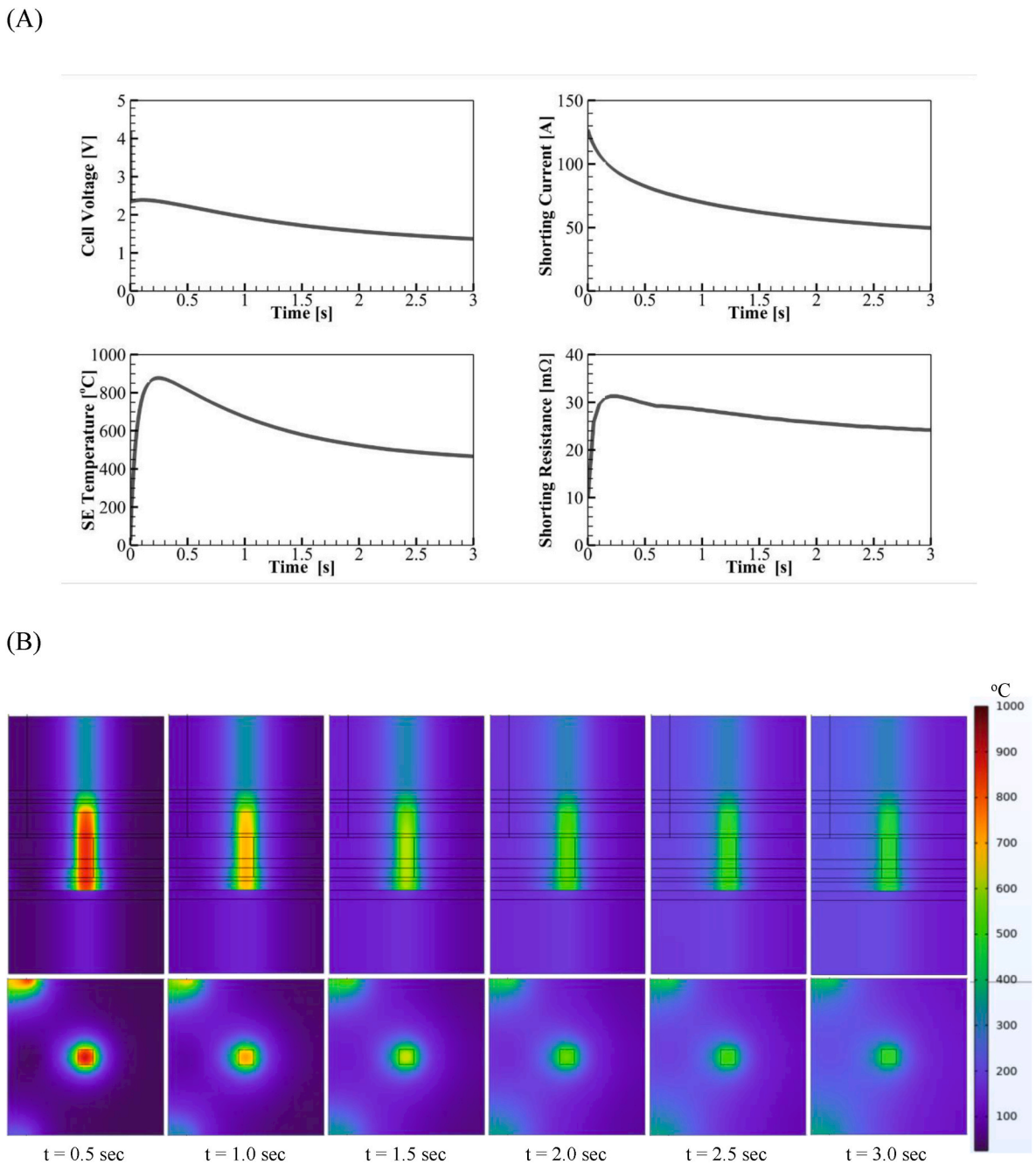

Fig. 4. Simulation results for the baseline case (shorted single-layer anode-free cell,4 × 4 mm SE @ centre, 2.6Ah ES) used for parametric study (A) Plots for various parameters (B) Temperature contours at different times (the left two corners are tab locations).

combined effects of increased ion transport, chemical kinetics, temperature and resistance lead to a recovery in voltage. Temperature data was difficult to match as they are highly localized and cannot be replicated precisely in experiments, and experimental cells involved extra thermal mass to be ignored in model simulation. Moreover, the temperature measured in the experiment was between two separator layers [28], whereas in the simulation, it was the volume average temperature of the SE. The data was matched only for a few seconds prior to the onset of fire and TR in the experiment and because of the lack of TR chemical kinetics modelling in the simulation. Total heat input, which is joule heat ($I_{SC}^2 R_{SC}$), and heating power (HP), which represents the rate of joule heat, were also matched.

3.2. Parametric study

The effect of cell design and cell chemistry on ISC was subsequently studied through a parametric study. A baseline case was chosen to compare the results of all the studies. The reference case includes the ISC of a single-layer AFB in parallel to the 2.6 Ah LiB ES. The single-layer cell was charged to 100 % SOC, and a short element of 4 × 4 mm was modelled at the centre, shorting anode CC to cathode CC. Fig. 4A shows various plots for the ISC of the baseline case. The voltage drop and shorting current are higher compared to the validation simulation, as the initial shorting resistance is only 10 mΩ. As the SE is just a small filament of very small dimensions, the temperature jump for SE is high but lasts for less than 1 s as the heat dissipates from the SE to the cell layers. The shorting resistance also increases instantaneously as it

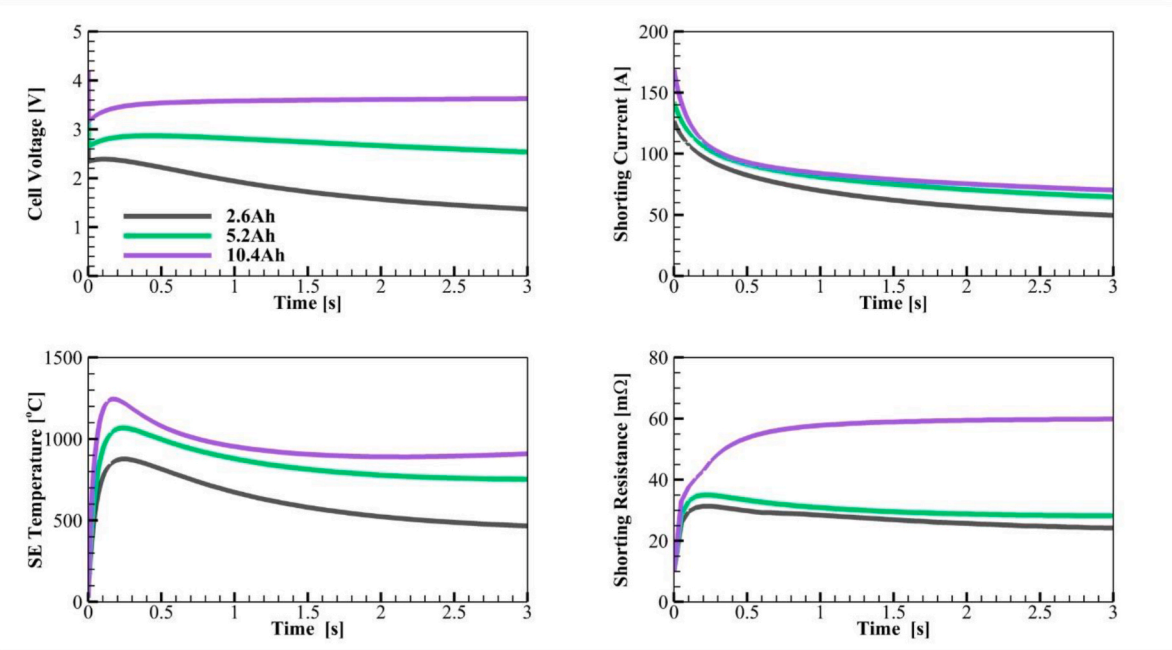

Fig. 5. Simulated effect of total cell capacity.

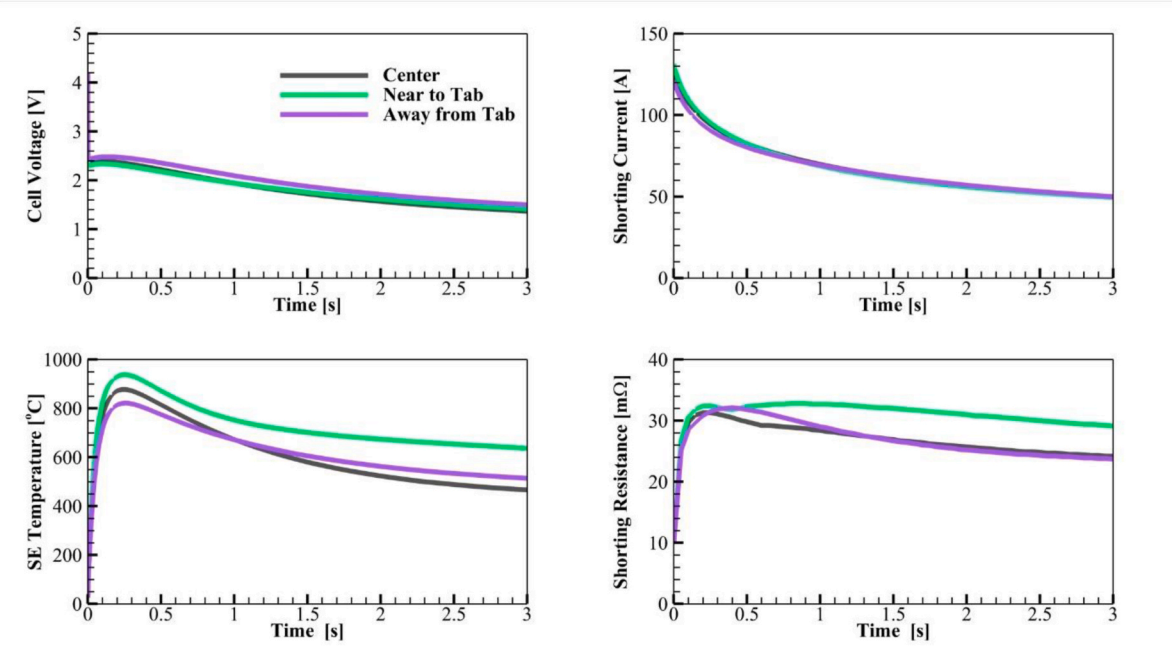

Fig. 6. Simulated effect of short location.

directly depends on temperature but, later on, decreases as the temperature decreases. The voltage drop profile matches the present literature [29], which is an initial drop followed by a little regain due to temperature and continuing to decrease till the cell is compromised. Fig. 4B shows the temperature contours for the single-layer cell at different times after shorting. The centre hot spot is the SE region, and two more hot spots in the corners are the tabs of the cell. As the ES supplies a large current to the single-layer cell, the tabs also generate a lot of joule heat.

3.2.1. *Effect of cell capacity*

The total cell capacity was increased by increasing the capacity of the energy source, mimicking the addition of more electrode layers in a battery in reality. A larger capacity ES supplies more current for the same initial shorting resistance. More current leads to more joule heating and a higher temperature for the shorting element. As the cell's capacity was higher, less voltage drop was needed for the same value of shorting resistance. Fig. 5 shows various plots for the effect of total cell capacity. At higher temperatures, the voltage regains is more, therefore, for 10.4 Ah ES, the voltage jumps back to a larger value soon after shorting. 10.4 Ah shorting case sees the most increase in the shorting resistance because of the highest temperature. As demonstrated experimentally in Ref. [28], the higher the initial shorting current, the more prone the battery will catch fire. Therefore, the present simulation

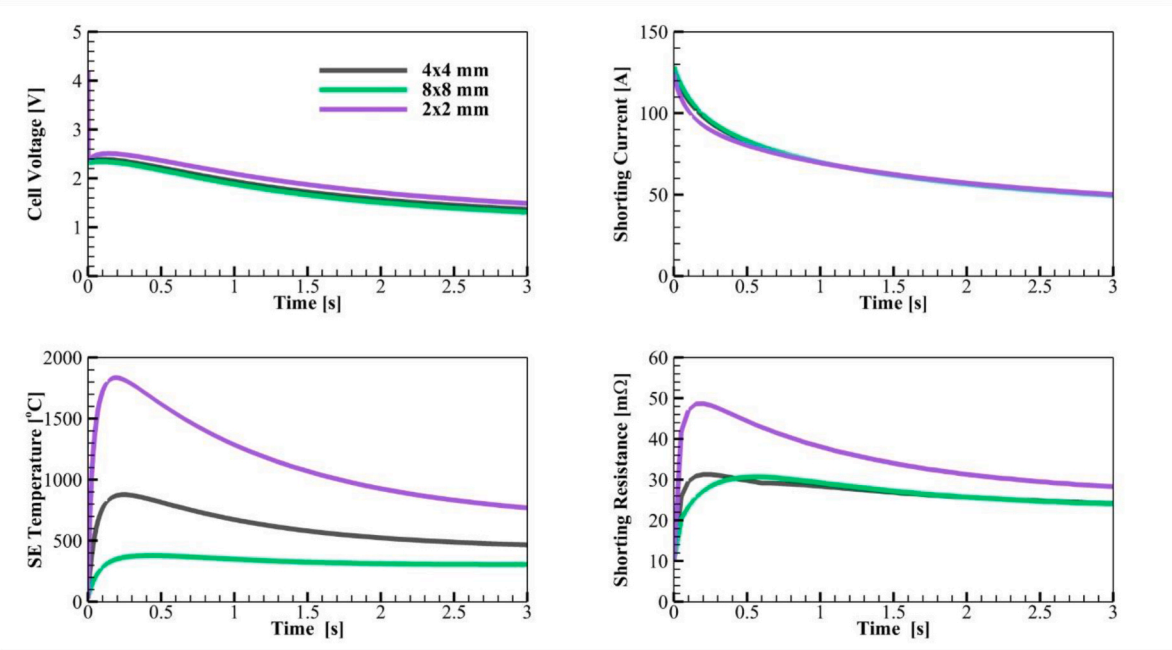

Fig. 7. Simulation results for the effect of short element size.

clearly indicates that the larger a cell, the more susceptible it will undergo thermal runaway.

3.2.2. *Effect of short location*

As the short location moves away from the tab, the total resistance of the current path increases, which leads to less current and less voltage drop during an ISC. Fig. 6 shows similar observations from the effect of short location simulation. The difference in voltage drop is in millivolts, but the current differs by 3–5 A. The impact of more current can be seen from temperature plots where near tab SE has a higher temperature, indicating more heat generation. Even though the temperature near tab SE is higher, the shorting resistance for 0.5 s shows similar trends for all three cases. Temperature contours in Fig. S5 can explain this trend. Temperature distribution is different for these cases, which leads to varying resistances for the current path. The current path is shortest for near to tab ISC followed by centre ISC and then away from tab ISC. As the current path for away from tab ISC is highest, the joule heat in this case is highest, which makes the total shorting resistance comparable to near to tab ISC.

3.2.3. *Effect of short element size*

Changing the short element (SE) size changes its thermal characteristics and the area it affects. Fig. 7 shows that the initial voltage drop and initial short-circuit current for all three cases are the same because

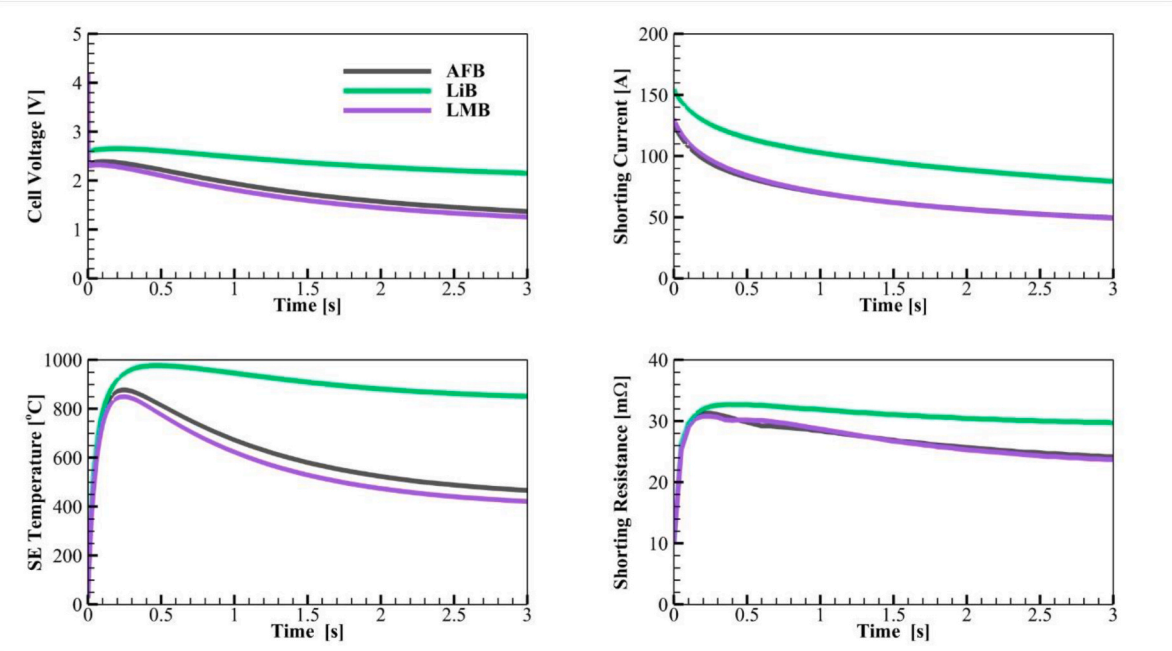

Fig. 8. Simulation results for the effect of anode.

the shorting resistance is the same. Soon after ISC, the temperature of the smallest SE rose to 1700 °C, which made the voltage gain for this case slightly higher than that of others. But, because of this temperature increase, the shorting resistance for this 2 × 2 mm shorting also becomes highest, which affects the short-circuit current, making it the least of the three. The short element temperature for 8 × 8 mm shorting is the lowest, but it has a broader area, which affects much more of the area of CCs, increasing the overall temperature of the cell. A larger current and a wider area of SE affect the cell tab, causing it to reach even higher temperatures. This high tab temperature creates more resistance for the current near the tabs, and the total shorting resistance for 8 × 8 mm shorting increases comparable to 4 × 4 mm shorting. Fig. S7 shows the temperature contours at 1 s after shorting and a higher temperature near tabs for 8 × 8 mm shorting.

3.2.4. Effect of anodes

Fig. 8 shows the effect of anode materials on ISC parameters. The direct current internal resistance (DCIR) of the single-layer cell affects the amount of current supplied by it during shorting, and as the DCIR for LiBs is the least, it supplies more current to the SE in addition to the current supplied by the ES. Even though AFB's DCIR is less than LMB's, their current is similar mainly because both have a high DCIR and supply a little current. The figure shows that the voltage drop of LiBs is the lowest because its DCIR is the lowest. As the shorting current for LiB is highest, the temperature is highest; hence, the shorting resistance increase is highest. The other two anode cases also follow trends based on temperature.

3.2.5. Effect of shorted layer SOC

Three cases with SOC 100 %, 75 % and 50 % were simulated to see the effect of SOC. As the single-layer AFB cell supplies very little short-circuit current, the SOC of the single-layer cell does not affect terminal voltage, shorting current, temperature and shorting resistance. The simulations produced the same results as Fig. 4a with a little difference between the three cases, and hence, plots are not presented for this case. Even though the ISC result parameters do not differ for this study, the TR will produce different results because of the effect of SOC on a cathode's ability to release oxygen, which is necessary for combustion reactions during TR [28]. Different SOC cells will have different amounts of Li at the anode and cathode, resulting in different reactions during a TR and, hence, different exothermic heat releases [30]. This suggests that the temperatures before initiation of TR side reactions are governed by ISC joule heat, and it is the cell chemistry, availability of chemicals and chemical reactions taking place at higher temperatures which govern the TR of a cell. This effect will be addressed in a future modelling study.

4. Conclusion

We have presented an ISC simulation model which can be validated from experimental data. Terminal voltage, short-circuit current, shorting resistance, temperature, and other derived parameters can be validated with experimental results using the simulation model and experimental technique presented here. The idea of studying the short layer as a separate cell makes this technique flexible for a parametric study and computationally inexpensive. The shorted layer, which is modelled using the chemistry of interest, is simulated with a finer mesh, and the un-shorted layers, which only work to supply current to the shorted layer, are simulated using a coarser mesh. The base case simulation result showed that with the onset of ISC, a large current inrush is seen, which is dependent on shorting resistance and cell capacity. The high shorting current gave rise to high joule heat, which suddenly raised the temperature of the short area. The effect of cell design and shorting parameters was seen on the short-circuit. The study of the effect of short location and short size showed that the short-circuit current highly depends on total shorting resistance, which changes during shorting due to increased resistances of current collectors because of local high temperatures. The effect of changing the anodes and SOC of the shorted single-layer turned out to produce a small effect on the shorting current and temperature evolution prior to the TR onset. The effect of total cell capacity proved to be most prominent and can be used to extend the results to a full-size car battery. Future applications of this model can include heat generation during reactions of various cell layers at higher temperatures. This can be possible by solving the Arrhenius-type rate equations for various sets of chemical reactions that occur during a TR. This method can help in predicting the onset of TR by simulating the effect of various side reactions for various parametric studies presented in this work.

CRediT authorship contribution statement

Nitesh Gupta: Writing – review & editing, Writing – original draft, Formal analysis, Data curation, Conceptualization. **Shanhai Ge:** Writing – original draft, Validation, Data curation. **Tatsuro Sasaki:** Validation, Data curation. **Kaiqiang Qin:** Writing – original draft, Conceptualization. **Ryan S. Longchamps:** Validation. **Koichiro Aotani:** Supervision, Project administration. **Chao-Yang Wang:** Project administration.

Declaration of competing interest

The authors declare that they have no known competing financial interests or personal relationships that could have appeared to influence the work reported in this paper.

Acknowledgements

Financial support from Nissan Motor Co. Ltd. is gratefully acknowledged. Software access and support from Gamma Technologies for GT-Autolion is greatly acknowledged.

Appendix A. Supplementary data

Supplementary data to this article can be found online at https://doi.org/10.1016/j.etran.2024.100380.

Data availability

Data will be made available on request.

References

[1] Liu B, Zhang JG, Wu X. Advancing lithium metal batteries. Joule 2018;2:833–45. https://doi.org/10.1016/j.joule.2018.03.008.
[2] Shen X, Liu H, Cheng XB, Yan C, Huang JQ. Beyond lithium ion batteries: higher energy density battery systems based on lithium metal anodes. Energy Storage Mater 2018;12:161–75. https://doi.org/10.1016/j.ensm.2017.12.002.
[3] Nanda S, Gupta A, Manthiram A. Anode-free full cells: a pathway to high-energy density lithium-metal batteries. Adv Energy Mater 2021;11:2000804. https://doi.org/10.1002/aenm.202000804.
[4] Deng J, Bae C, Denlinger A, Miller T. Electric vehicles batteries: requirements and challenges. Joule 2020;4:511–5. https://doi.org/10.1016/j.joule.2020.01.013.
[5] Wu Y, Xie L, Ming H, Guo Y, Hwang JY, Wang W, et al. An empirical model for the design of batteries with high energy density. ACS Energy Lett 2020;5:807–16. https://doi.org/10.1021/acsenergylett.0c00211.
[6] Xu W, Wang J, Ding F, Chen X, Nasybulin E, Zhang Y, et al. Lithium metal anodes for rechargeable batteries. Energy Environ Sci 2014;7:513–37. https://doi.org/10.1039/C3EE40795K.
[7] Wang CY, Liu T, Yang XG, Ge S, Stanley NV, Rountree ES, et al. Fast charging of energy-dense lithium-ion batteries. Nature 2022;611:485–90. https://doi.org/10.1038/s41586-022-05281-0.
[8] Guo Z, Cui Z, Sim R, Manthiram A. Localized high-concentration electrolytes with low-cost diluents compatible with both cobalt-free LiNiO2 cathode and lithium-metal anode. Small 2023;19:2305055. https://doi.org/10.1002/smll.202305055.
[9] Puthusseri D, Parmananda M, Mukherjee PP, Pol VG. Probing the thermal safety of lithium metal batteries. J Electrochem Soc 2020;167:120513. https://doi.org/10.1149/1945-7111/ababd2.
[10] Lu B, Cheng D, Sreenarayanan B, Li W, Bhamwala B, Bao W, et al. Key parameters in determining the reactivity of lithium metal battery. ACS Energy Lett 2023;8:3230–8. https://doi.org/10.1021/acsenergylett.3c01001.

[11] Wang L, Zhou Z, Yan X, Hou F, Wen L, Luo W, et al. Engineering of lithium-metal anodes towards a safe and stable battery. Energy Storage Mater 2018;14:22–48. https://doi.org/10.1016/j.ensm.2018.02.014.
[12] Qian L, Or T, Zheng Y, Li M, Karim D, Cui A, et al. Critical operation strategies toward high-performance lithium metal batteries. Renewables 2023;1:114–41. https://doi.org/10.31635/renewables.023.202200014.
[13] Gao X, Zhou YN, Han D, Zhou J, Zhou D, Tang W, et al. Thermodynamic understanding of Li-dendrite formation. Joule 2020;4:1864–79. https://doi.org/10.1016/j.joule.2020.06.016.
[14] Liu Y, Mao Y, Wang H, Pan Y, Liu B. Internal short circuit behaviors of lithium metal batteries under mechanical abuse loading. Int J Mech Sci 2013;245:108130. https://doi.org/10.1016/j.ijmecsci.2023.108130.
[15] Mao B, Chen H, Cui Z, Wu T, Wang Q. Failure mechanism of the lithium ion battery during nail penetration. Int J Heat Mass Tran 2018;122:1103–15. https://doi.org/10.1016/j.ijheatmasstransfer.2018.02.036.
[16] Finegan DP, Tjaden B, Heenan TMM, Jervis R, Michiel MD, Rack A, et al. Tracking internal temperature and structural dynamics during nail penetration of lithium-ion cells. J Electrochem Soc 2017;164:A3285–91. https://doi.org/10.1149/2.1501713jes.
[17] Lamb J, Orendorff CJ. Evaluation of mechanical abuse techniques in lithium ion batteries. J Power Sources 2014;247:189–96. https://doi.org/10.1016/j.jpowsour.2013.08.066.
[18] Liu S, Huang S, Zhou Q, Snyder K, Long MK, Zhang G. In situ measurement of dynamic internal short circuit resistance during nail penetration of lithium-ion cells and its implications on cell robustness and abuse tolerance. J Electrochem Soc 2023;170:060515. https://doi.org/10.1149/1945-7111/acd814.
[19] Finegan DP, Darcy E, Keyser M, Tjaden B, Heenan TMM, Jervis R, et al. Characterising thermal runaway within lithium-ion cells by inducing and monitoring internal short circuits. Energy Environ Sci 2017;10:1377–88. https://doi.org/10.1039/C7EE00385D.
[20] Lopez CF, Jeevarajan JA, Mukherjee PP. Experimental analysis of thermal runaway and propagation in lithium-ion battery modules. J Electrochem Soc 2015;162:A1905–15. https://doi.org/10.1149/2.0921509jes.
[21] Doughty D, Roth EP. A general discussion of Li ion battery safety. Electrochem Soc Interface 2012;21:37–44. https://doi.org/10.1149/2.F03122if.
[22] Zhao W, Luo G, Wang CY. Modeling nail penetration process in large-format Li-ion cells. J Electrochem Soc 2014;162:A207. https://doi.org/10.1149/2.1071501jes.
[23] Zhao R, Liu J, Gu J. Simulation and experimental study on lithium ion battery short circuit. Appl Energy 2016;173:29–39. https://doi.org/10.1016/j.apenergy.2016.04.016.
[24] Zavalis TG, Behm M, Lindbergh G. Investigation of short-circuit scenarios in a lithium-ion battery cell. J Electrochem Soc 2012;159:A848. https://doi.org/10.1149/2.096206jes.
[25] Liu T, Ge S, Yang XG, Wang CY. Effect of thermal environments on fast charging Li-ion batteries. J Power Sources 2021;511:230466. https://doi.org/10.1016/j.jpowsour.2021.230466.
[26] Jia H, Xu Y, Burton SD, Gao P, Zhang X, Matthews BE, et al. Enabling ether-based electrolytes for long cycle life of lithium-ion batteries at high charge voltage. ACS Appl Mater Interfaces 2020;12:54893–903. https://doi.org/10.1021/acsami.0c18177.
[27] Valøen LO, Reimers JN. Transport properties of LiPF6-based Li-ion battery electrolytes. J Electrochem Soc 2005;152:A882. https://doi.org/10.1149/1.1872737.
[28] Ge S, Sasaki T, Gupta N, Qin K, Longchamps RS, Aotani K, et al. Quantification of lithium battery fires in internal short circuit. ACS Energy Lett 2024;9:5747–55. https://doi.org/10.1021/acsenergylett.4c02564.
[29] Long MK, Liu S, Zhang G. A novel method for simultaneous triggering and in situ sensing of internal short circuit in lithium-ion cells. Energy Advances 2023;2:2018–28. https://doi.org/10.1039/D3YA00311F.
[30] Hou J, Lu L, Ohma A, Ren D, Feng X, Li Y, et al. Thermal runaway of Lithium-ion batteries employing LiN $(SO_2F)_2$-based concentrated electrolytes. Nat Commun 2020;11:5100. https://doi.org/10.1038/s41467-020-18868-w.